Grazing incidence X-ray diffraction spectra analysis of expanded austenite for implanted stainless steel

J. Dudognon, M. Vayer *, A. Pineau, R. Erre

Centre de Recherche sur la Matiere Divisée, 1b rue de la Ferollerie, 45071 Orleans Cedex 2, France

ARTICLE INFO

ABSTRACT

This work proposed to investigate the structure of the modified austenite fcc phase due to ion implantation and called "expanded austenite" using grazing incidence angle X-ray diffraction (GIXRD) measurements combined with the application of a model for simulating X-ray diffraction peaks. Ion implantation of different atomic elements (N, Cr, Mo, Ag, Xe and Ar) have been carried in the near surface region of an austenitic 316LVM stainless steel (the implanted layer thickness did not exceed 60 nm). Mild ion implantation conditions were chosen to avoid the structural transformation of the steel: no ferrite and no amorphous phase were formed. The structure of the implanted layers was investigated by GIXRD at different incidence angles. A original model was proposed to simulate the X-Ray diffraction peaks. This model took into account the incidence angle, the ion implantation conditions (fluence and energy) through the concentration depth profile and finally the nature of the implanted ion through a k coefficient. All the recorded X-ray diffraction peaks were simulated with this model.

© 2008 Elsevier B.V. All rights reserved.

1. Introduction

Ion implantation of austenitic stainless steel induces chemical and structural modifications of the steel in the implanted layer which, depending on ion implantation conditions, undergoes several types of transformation: expansion of the austenite [1,2] with the appearance of a new austenitic phase generally called expanded austenite, appearance of new phases: ferrite or nitride [3–5] and amorphisation [6–8]. The expansion of austenite and the nature of expanded austenite in particular in the case of nitriding were largely explored by X-ray diffraction. However, interpretations drawn from the observed diffractograms are not all convergent. In fact, the structure of expanded austenite has been interpreted in different ways and remains under controversy [3,9–14]. The goal of this work is to investigate using GIXRD the structure of expanded austenite. An austenitic stainless steel was thus implanted with several elements with different properties – miscible elements: chromium and molybdenum which substitute steel elements and nitrogen which goes in insertion in the lattice, – immiscible elements: metallic

elements which are not soluble in austenitic steel such as silver and rare gases: argon and xenon. The implanted ions were also chosen to have a wide range of radii, smaller or larger than the steel elements ones. The implantation conditions (energy and fluence) were chosen to limit the transformation of implanted layer and to form at the most small amount of ferrite. Moreover, the conditions are selected in order to have an implanted element concentration enough to be detected by Rutherford backscattering spectrometry (RBS) and to enable observable modifications in grazing incidence X-Ray diffraction (GIXRD). The structure of the implanted layer was explored using GIXRD at different incidence angles. Theoretical diffractograms were constructed using the method proposed in a previous paper for Mo-implanted austenitic steel [14], compared and adjusted to the recorded experimental ones. New insights into interpretation of X-ray diffraction spectra of expanded austenite will be given.

2. Materials and methods

2.1. Materials

The material used in this study was AISI 316LVM cold-rolled stainless steel which atomic composition is 18.71 Cr, 13.08 Ni, 1.72 Mn, 1.61 Mo, 1.03 Si, 0.29 N, 0.07 C, 0.04 P and balance Fe. Samples cut from

---

* Corresponding author.
E-mail address: marylene.vayer@univ-orleans.fr (M. Vayer).

a bar were mechanically polished up to obtain a mirror-like surface with a 2 nm (rms) roughness. Its density was 7.922. This steel presented an austenitic structure with a lattice parameter a_0 in bulk of 0.36002 nm.

2.2. Ion implantation

Ion implantations were performed at room temperature in CSNSM (Orsay, France) in the accelerator IRMA with the isotopic separator SIDONIE. The ion implantation conditions led to truncated Gaussian element concentration depth profiles with maximal atomic concentration C_{max} at R_p (Table 1).

Samples were implanted with N, Cr, Ar, Xe, Mo and Ag at an ion acceleration energy to keep the implanted element depth profile close to a R_p of 25 nm. A fluence of $2 \cdot 10^{16}$ ions cm^{-2} was used for N, Cr, Ar and Xe to have C_{max} close to 7%. Mo and Ag ion implantation were performed with different fluences and energy.

2.3. Grazing incidence X-ray diffraction

2.3.1. Recording the diffractograms

The crystallographic structure of the implanted layer was characterized by asymmetric in plane Grazing Incidence X-ray diffraction (GIXRD) using a Philips X'pert parallel horizontal beam diffractometer. Cu Kα (λ = 1.54056 Å) source was used as incident beam. Incidence angles were between 0.4° and 3.0°. The peak positions were evaluated after correction of refraction effect due to grazing incidence. Angles were measured with a 0.03° precision that means $5 \cdot 10^{-4}$ nm precision for the lattice parameter. The diffractograms were first recorded for 2θ diffraction angles between 35 and 95° and then more precisely between 72 and 76°. For the samples which are composed of austenite and ferrite, the relative proportion of ferrite P_f was determined with the ratio of the intensities of the X-ray diffraction peaks $\gamma(111)$ and $\alpha(110)$ at 0.5° incidence angle corrected by the theoretical ratio between the two peaks.

2.3.2. Simulating the austenite X-ray diffraction peak

The austenitic $\gamma(220)$ peak was chosen to be simulated here since this peak is relatively intense and its position (2θ) at 74.5° has two advantages. There is no influence of another peak and the lattice parameter increase due to $\sin\theta$, i.e. small changes in lattice parameter induces larger changes in 2θ, has a higher effect than for other peaks at lower positions. Stresses (uniform or/and non uniform) have an effect on peak position and on peak shape. The $\gamma(220)$ peak correspond to an angle of $\approx 36.5°$ between the diffraction vector and the surface. If we assume a Poisson's ratio for stainless steel of 0.3, the value for the angle at which the stress free lattice parameter occurs is when the diffraction angle is at 42.8° to the surface. The $\gamma(220)$ peak is near the stress free position and consequently the stresses effect on this peak is very weak.

Table 1
Ion implantation conditions: R_p depth of the maximal concentration, maximal concentration C_{max}, P_f ferrite amount in the implanted layer

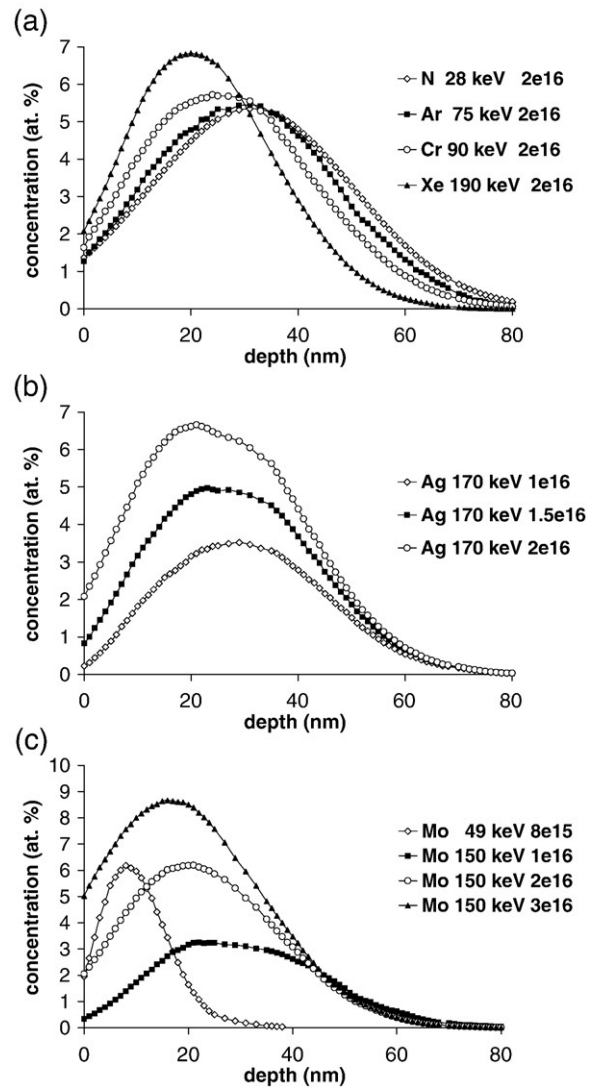| Ion	Energy (keV)	Fluence (ions cm^{-2})	R_p (nm)	C_{max} (at.%)	P_f (%)
N	28	$2 \cdot 10^{16}$	31	5.4	–
Ar	75	$2 \cdot 10^{16}$	29	5.5	–
Cr	90	$2 \cdot 10^{16}$	25	5.7	–
Xe	190	$2 \cdot 10^{16}$	21	6.8	30
Ag	170	$1 \cdot 10^{16}$	27	3.5	–
		$1.5 \cdot 10^{16}$	26	4.9	–
		$2 \cdot 10^{16}$	21	6.6	9
Mo	49	$8 \cdot 10^{15}$	8	6.2	–
	150	$1 \cdot 10^{16}$	22	3.3	–
		$2 \cdot 10^{16}$	21	6.1	10
		$3 \cdot 10^{16}$	16	8.7	16

Fig. 1. Element concentration depth profiles as calculated for implanted samples presented in Table 1. N, Ar, Cr, Xe implantation (a); Ag implantation (b); Mo implantation (c).

The austenitic $\gamma(220)$ peak obtained with GIXRD were simulated following a procedure proposed in a previous paper for Mo-implanted austenitic steel [14].
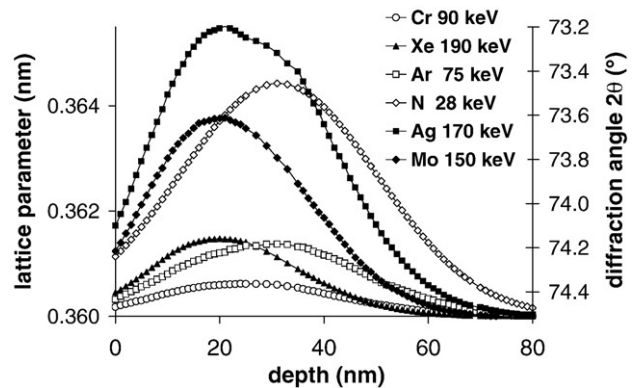

Fig. 2. Lattice parameter $a(z)$ depth profiles for implantation of $2 \cdot 10^{16}$ ions cm^{-2} of Cr at 90 keV (k = 0.03); Xe at 190 keV (k = 0.06); Ar at 75 keV (k = 0.07); Mo at 150 keV (k = 0.15); N at 28 keV (k = 0.17); Ag at 170 keV (k = 0.23) (a_0 = 0.3597 nm).
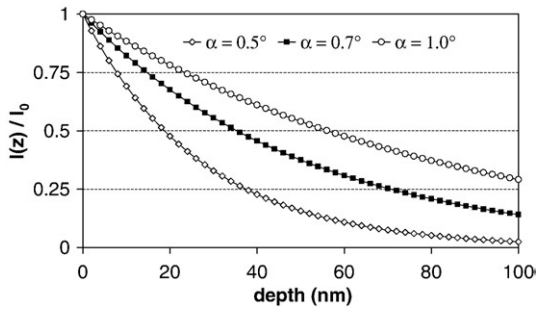
Fig. 3. Relative intensity (I/I_0) of diffracted X-ray signal for a 316LVM stainless steel versus depth for α=0.5, 0.7 and 1.0°.

The different steps and assumptions are summarized here:

1. The ion concentration depth profile $c(z)$ was known. The implanted ion concentration $c(z)$ as a function of depth z was non uniform and was simulated using the probability of presence of implanted ion as a function of depth and the ion sputtering coefficient determined by SRIM2003 computer program [15]. The simulated concentration depth profiles were confirmed by RBS. Fig. 1 presents concentration depth profiles for the implanted samples displayed in Table 1.
2. The lattice parameter $a(z)$ at the depth z was supposed to be linearly linked to the atomic fraction $c(z)$ of the implanted element at the depth z following: $a(z)=a_0*(1+k*c(z))$ where a_0 is the original lattice parameter. This relationship could be linked to the difference of atomic volume between substituted steel element and substituting implanted element as in a Vegard law [16,17] or to insertion of implanted element into the lattice (N or H), and to the stresses or defects induced by ion introduction [18,19]. Both effects have to be considered. Lattice parameter depth profile $a(z)$ was established supposing the value of k as shown on Fig. 2. The effects of texture, grain size are not taken in consideration. This profile was converted in diffraction angle depth profile $2\theta(z)$ through the Bragg law (Fig. 2).
3. The intensity of diffracted X-rays decreased with the origin depth in matter following an exponential law. The intensity of X-rays beam $I(z)$ at a depth z was defined by $I(z)=I_0*\exp(-\tau*z)$ where I_0 is the intensity of X-ray beam impinging on the sample and an τ is the absorption function which depends on the incidence angle α. τ is calculated using Fresnel's and Snell's laws. As the incidence angle was less than 3°, the absorption of the diffracted beam in matter was negligible compared to those of incident beam. Consequently, τ only depended on the incident angle α ($1/\tau$ called information depth equals 27, 51 and 81 nm respectively for 0.5, 0.7, 1.0°). The relative intensity of X-ray diffracted

signal as a function of the depth is represented in Fig. 3 for the incidence angles used.

4. The theoretical spectrum $I(\theta)$ was constructed by convolution of the inverse of diffraction angle depth profile $2\theta(z)$, the X-ray intensity depth profile $I(z)$ and to the instrumental broadening function. This latter function was determined by recording the diffracted X-ray peaks of a polycrystalline silicon sample at the used incidence angles and in the same diffraction angles range that the studied steel X-ray diffracted peaks. The X-ray Si γ(311) peak which appears at 2θ=76° was chosen for the simulation of the 316LVM stainless steel γ(220) peak (2θ=74°). Examples of theoretical spectra obtained is shown in Fig. 4 for the γ(220) peak of austenite. The signal coming from the implanted layer had a higher intensity than the signal coming from the volume for an incident diffraction angle of 0.5°. The opposite was observed for 1° incidence angle. With a continuous repartition of element into the implanted layer, the X-ray peak presented completely different shapes depending on α. In grazing incidence X-ray diffraction, the diffraction peak shape can be confusing and two peak components have not to be systematically attributed to the presence of two different phases but can be due to a continuous variation of lattice parameter. Unambiguous interpretation of X-ray diffractograms needs the records of at least 2 or 3 diffractograms at different incidence angles.
5. The calculated spectra were compared with experimental spectra. A Fortran program was written to construct theoretical spectrum $I_{cal}(\alpha,\theta)$ knowing the incidence angle α, the original lattice parameter a_0, the implanted ion depth profile $c(z)$ and the k coefficient. The reconstructed spectrum was adjusted to the experimental spectrum $I_{exp}(\alpha,\theta)$ using a least squares minimization method by varying the k coefficient.
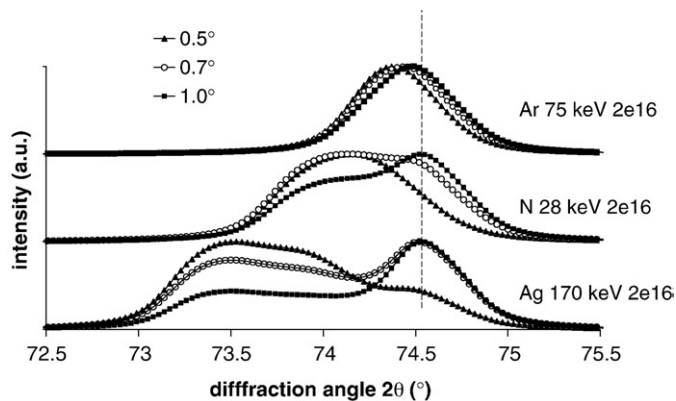

Fig. 4. Theoretical spectra of the γ(220) peak of 316LVM steel implanted with $2\cdot10^{16}$ ions cm^{-2} of Ar at 75 keV (k=0.07), N at 28 keV (k=0.17) and Ag at 170 keV (k=0.23) (a_0=0.3597 nm) for α=0.5, 0.7 and 1.0°.
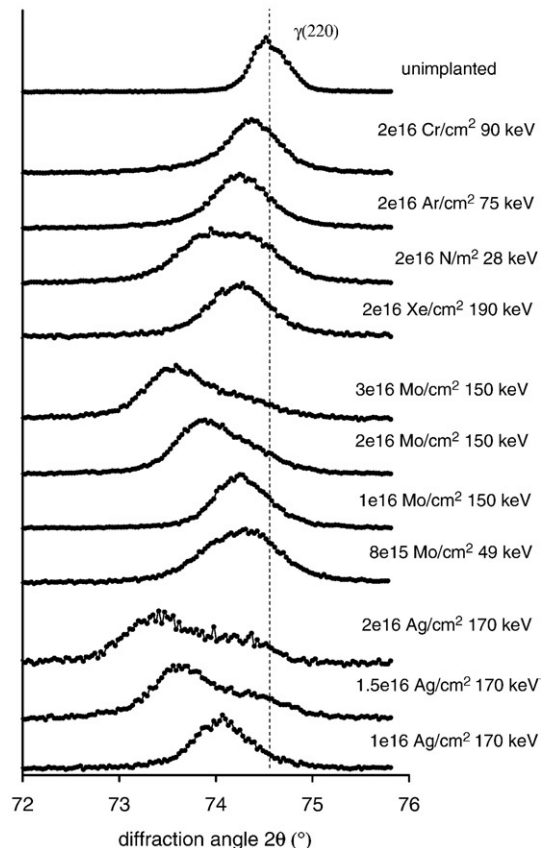

Fig. 5. X-ray diffraction spectra of the 2θ region for unimplanted and implanted samples between 40 and 80° for 0.5° incidence angle.

The quality of the adjustment was evaluated through a correlation factor f_c defined as

$$f_c = \sqrt{\frac{\sum_\theta \left((I_{cal}(\alpha,\theta))^2 - (I_{moy}(\alpha))^2 \right)}{\sum_\theta \left((I_{exp}(\alpha,\theta))^2 - (I_{moy}(\alpha))^2 \right)}}$$

where $I_{moy}(\alpha)$ is the average intensity over the considered peak. The adjustment was reasonable when f_c was greater than 0.98.

3. Results

3.1. Structural modifications induced by ion implantation

At 0.5° incidence angle and within the selected experimental conditions, ion implantation induced mainly modification austenite peaks in shape and in position (Fig. 5). Small amounts of ferrite were observed as put in evidence by the presence of $\alpha(110)$ peaks in the 2θ range 44–45° in some cases as for Mo at $3 \cdot 10^{16}$ ions cm^{-2} at 150 keV (Fig. 5). The experimental conditions were voluntarily restricted to ones where no amorphisation was observed and less than 30% of ferrite was formed in implanted layer (Table 1). Fig. 6 displays the $\gamma(220)$ peak for an incidence angle of 0.5° and the selected ion implantation conditions. Ion implantation induces a broadening and/or a shift of austenite peaks towards lower diffraction angles (see as example $2 \cdot 10^{16}$ Cr cm^{-2} at 90 keV), and in some cases splitting of the peak into two components, one at the peak position of the unimplanted sample and the other at a lower
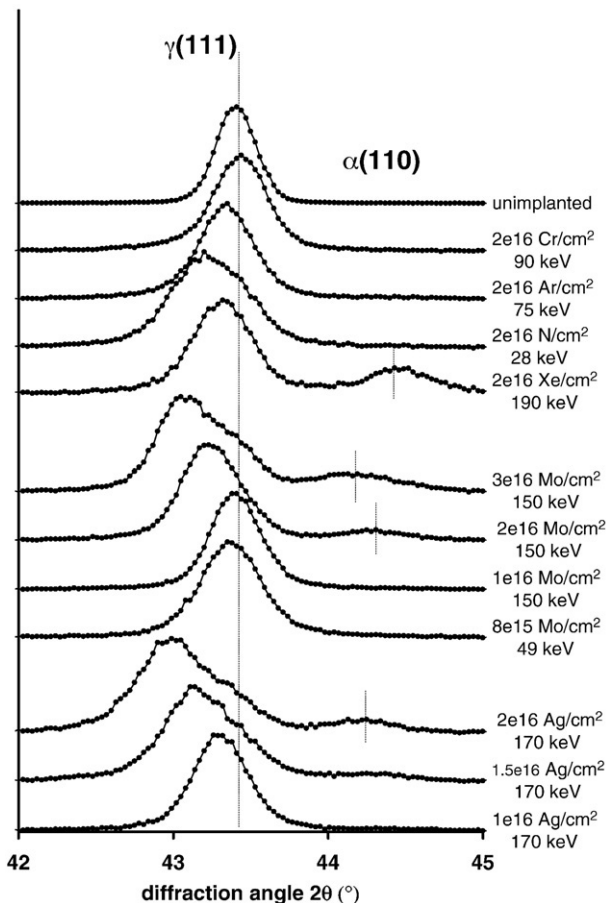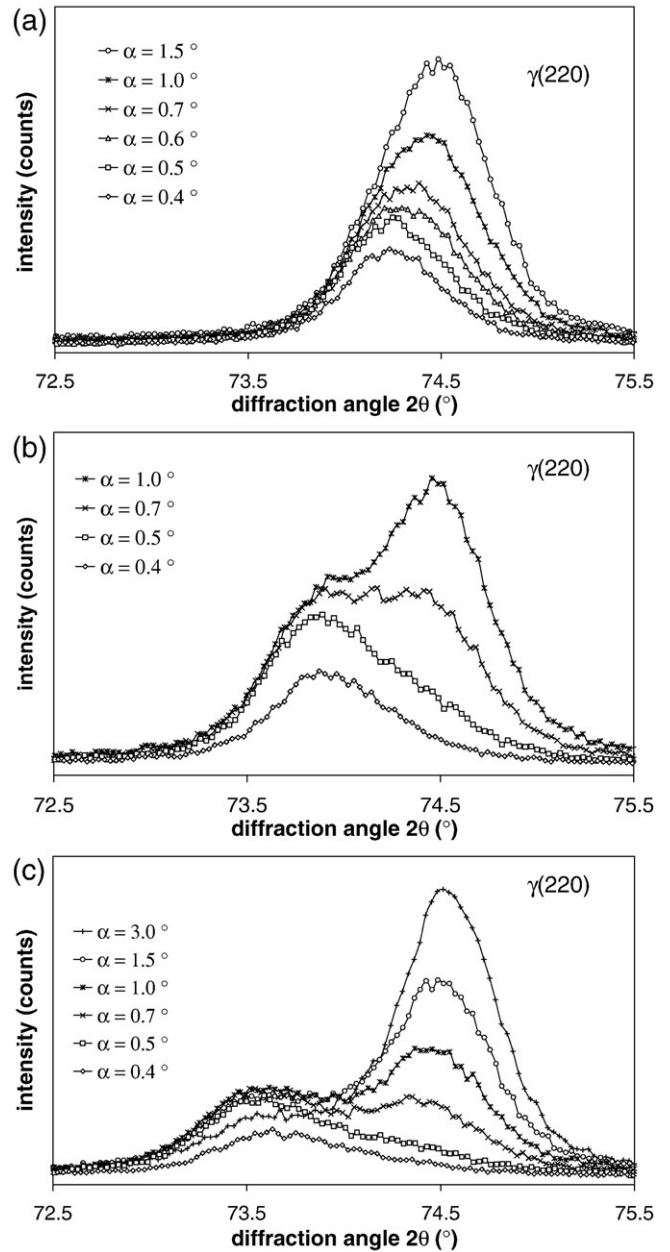

Fig. 7. Experimental $\gamma(220)$ peaks of 316LVM stainless steel implanted with $1 \cdot 10^{16}$ Mo cm^{-2} (a), $2 \cdot 10^{16}$ Mo/cm^{2} (b), $3 \cdot 10^{16}$ Mo cm^{-2} (c) at 150 keV at different incidence angles.

diffraction angle position (see as example $2 \cdot 10^{16}$ N cm^{-2} at 28 keV). The austenite transformation depended – on the implanted element (compare N at 28 keV, Cr at 90 keV and Ag at 170 keV same concentration depth profile, same fluence ($2 \cdot 10^{16}$ ions cm^{-2}) and adapted energy) – on the fluence (compare Mo at 150 keV, for $1 \cdot 10^{16}$ ions cm^{-2}, $2 \cdot 10^{16}$ ions cm^{-2} and $3 \cdot 10^{16}$ ions cm^{-2}). Higher fluences went through deeper transformation as seen in Fig. 6 and Table 1.

As shown in Fig. 7, the shape of the $\gamma(220)$ peak at different incidence angles was strongly dependant on the incidence angle.

3.2. Simulation of the $\gamma(220)$ peak of implanted sample

For all the examined samples, implanted element concentration depth was known and austenite $\gamma(220)$ X-ray diffraction peaks

Fig. 6. X-ray diffraction spectra of the 2θ region for unimplanted and implanted samples between 72 and 76 for 0.5° incidence angle.

recorded at 0.5, 0.7 and 1° incidence angles were simulated with the procedure presented above by means of the adjustment of k. The results are presented in Figs. 8, 9 and Table 2. For all the examined samples within the selected conditions and incidence angles, f_c values were higher than 0.98. There is consequently an excellent agreement between experimental peaks and the simulated peaks. The proposed model was adequate to simulate the experimental peaks.

For each implantation condition (element, energy and fluence), the k coefficients for the 3 incidence angles (0.5, 0.7, 1) were similar. Thus, the k coefficient was independent of the incidence angle and the retained k value was the mean value of the three values for the incidence angles 0.5, 0.7 and 1.0°.

For Mo implantation at 150 keV and Ag implantation at 170 keV, the effect of the fluence was studied. The adjusted values for k were the same for the fluences $2 \cdot 10^{16}$ and $3 \cdot 10^{16}$ ions cm^{-2}. The values determined for $1 \cdot 10^{16}$ ions cm^{-2} were slightly weaker. Moreover,

the k coefficient for Mo 49 keV, $8 \cdot 10^{15}$ ions cm^{-2} was similar to the ones obtained at 150 keV (Table 2). From this observation we concluded that the k coefficient was independent of the incidence angle, of the ion fluence and ion energy and only dependent on the implanted element. This was only true when the major part of the implanted layer remained austenite. This model was based on the fact that the implanted element was in the austenite phase. When ferrite formation or amorphisation took place in the implantation layer, this was not true since implanted element was also incorporated to ferrite and amorphous phase.

4. Discussion

The k values determined by peak adjustment were compared to the ones given in the literature, which concern mainly N implantation and also to calculated theoretical values.

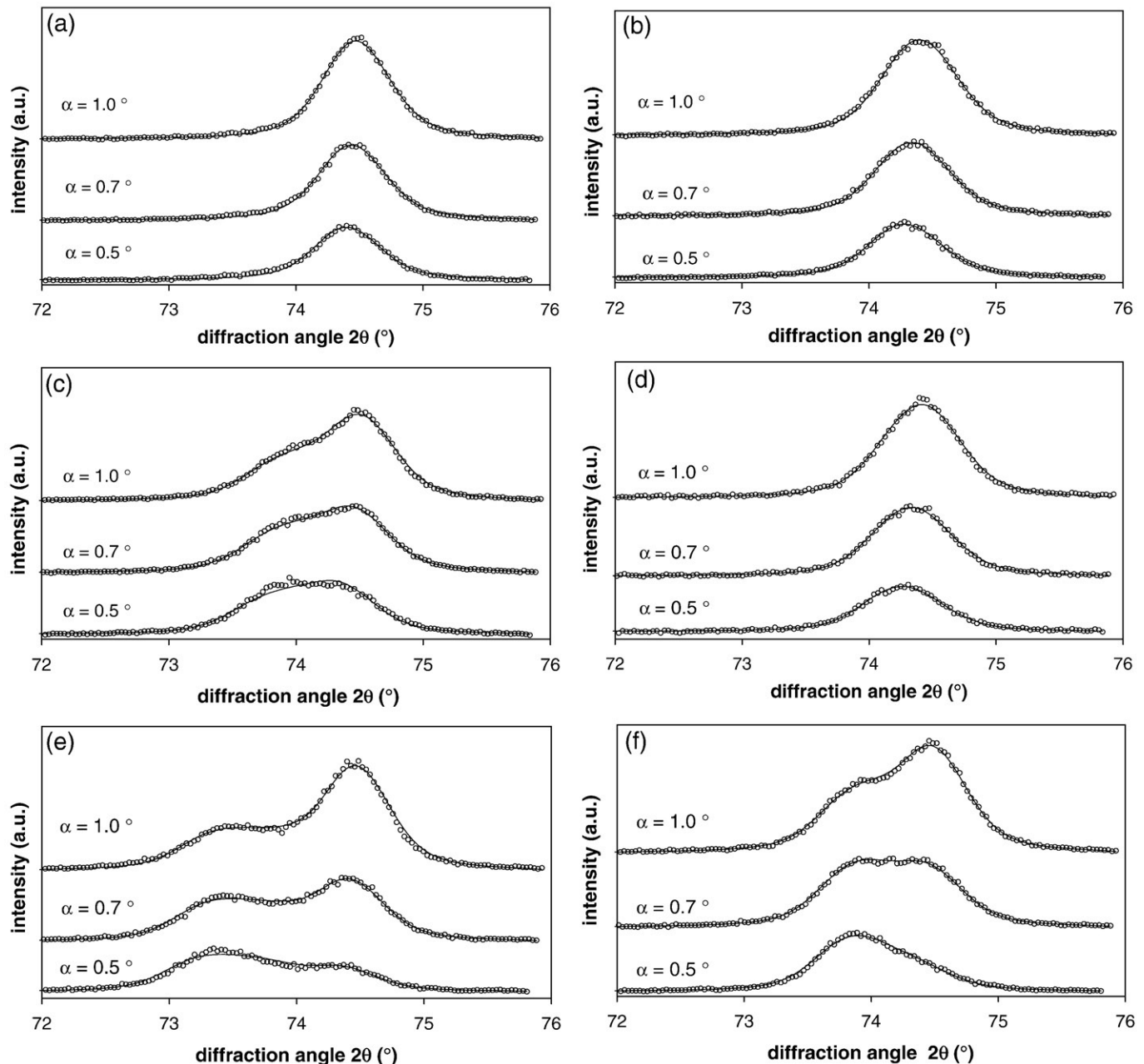**Fig. 8.** Theoretical and experimental γ(220) peaks at 0.5°, 0.7° and 1.0° for 316LVM implanted with $2 \cdot 10^{16}$ Cr cm^{-2} at 90 keV (a), $2 \cdot 10^{16}$ Ar cm^{-2} at 75 keV (b), $2 \cdot 10^{16}$ N cm^{-2} at 28 keV (c), $2 \cdot 10^{16}$ Xe cm^{-2} at 190 keV(d), $2 \cdot 10^{16}$ Ag cm^{-2} at 170 keV(e), $2 \cdot 10^{16}$ Mo cm^{-2} at 150 keV (f).

The implanted elements were divided in three classes.

– The first class was constituted by elements which are miscible in steel and which are small enough to go in insertion in octahedral site in the austenite lattice. A theoretical value was calculated using the relation $k_{theo}=4[(R+R_0)-2\sqrt{2}R]/R_0$, where R is the radius of the implanted element and R_0 the mean atomic radius of 316LVM stainless steel ($R_0=0.12714$ nm). This was the case of nitrogen ($R_N=0.075$ nm) which is well-known to go in insertion in steel, when it is in limited quantity. The calculated value of k_{theo} for nitrogen was 0.25. This value was close to the experimental one ($k_{exp}=0.17$) and in the same range than the experimental values between 0.17 and 0.30 reported in the literature (0.17 [22,23], 0.20 [5], 0.21 [24], 0.22 [2] 0.27 [25] 0.30 [6]).

– The second class was constituted by elements which are miscible in steel and form a substitution solid solution (Cr, Mo). k_{theo} was calculated following the relation $k_{theo}=(R-R_0)/R_0$ where R is the radius of the implanted element ($R_{Cr}=0.1288$ nm)and $R_{Mo}=0.1405$ nm) and R_0 the mean atomic radius of 316LVM stainless steel ($R_0=0.12714$ nm). The calculated values for Cr and Mo were respectively equal to 0.01 and 0.10. Experimental values were respectively equal to 0.03 and 0.15 and were close to the calculated values of k and to the ones given in the literature (0.0143 for Cr and 0.0843 for Mo [16]).

– The third class was constituted by immiscible elements which segregated in steel. The rare gas atoms Ar and Xe are known to form solid nanocrystallized precipitates when they are implanted

Table 2
k coefficients, correlation factors (f_c), mean values of the k coefficients k_{mean} determined by adjustment of the theoretical X-ray diffraction γ(220) peaks to the experimental ones

Element	Energy (keV)	Fluence (ions cm^{-2})	α (°)	k	f_c	k_{mean}
N	28	$2\cdot10^{16}$	0.5	0.172	0.984	0.17
			0.7	0.172	0.994	
			1.0	0.172	0.996	
Ar	75	$2\cdot10^{16}$	0.5	0.069	0.991	0.07
			0.7	0.069	0.997	
			1.0	0.069	0.997	
Cr	90	$2\cdot10^{16}$	0.5	0.033	0.997	0.03
			0.7	0.033	1.000	
			1.0	0.033	0.998	
Xe	190	$2\cdot10^{16}$	0.5	0.064	0.994	0.07
			0.7	0.064	0.997	
			1.0	0.064	0.999	
Mo	49	$8\cdot10^{15}$	0.5	0.155	0.976	0.15
			0.7	0.155	0.976	
			1.0	0.155	0.976	
	150	$1\cdot10^{16}$	0.5	0.128	0.991	0.12
			0.7	0.117	0.997	
			1.0	0.130	0.999	
		$2\cdot10^{16}$	0.5	0.139	0.992	0.14
			0.7	0.147	0.999	
			1.0	0.150	0.999	
		$3\cdot10^{16}$	0.5	0.139	0.996	0.14
			0.7	0.144	0.993	
			1.0	0.147	0.990	
Ag	170	$1\cdot10^{16}$	0.5	0.194	0.984	0.19
			0.7	0.192	0.992	
			1.0	0.197	0.996	
		$1.5\cdot10^{16}$	0.6	0.247	0.986	0.25
			0.7	0.255	0.989	
			1.0	0.247	0.998	
		$2\cdot10^{16}$	0.5	0.230	0.992	0.23
			0.7	0.225	0.999	
			1.0	0.225	0.997	

into metals [20,21]. Ag is immiscible in steel and form small nanoclusters when implanted in steel.

– Although, the simulated X-rays diffraction peaks are in good agreement with the experimental ones through a k coefficient, the effect of ion implantation could not reduced to the volume effect of implanted elements. Ion implantation induced indeed the presence of numerous defects or defects clusters (interstitial loops and vacancy loops, 3D interstitial clusters) [26,27] which were a source of internal stresses. The k coefficient results of the volume effect of implanted element but also of the damages induced by implantation.

5. Conclusion

The proposed model allowed the simulation of X-ray diffraction peaks at grazing incidence angles for expanded austenite fcc phase formed by ion implantation within selected implantation conditions (no amorphisation and limited ferrite formation). All the observed austenite peaks shapes resulted from the incidence angle, the ion implantation conditions (fluence and energy) through the concentration depth profile and finally from the nature of the implanted ion through a k coefficient. X-ray diffraction peaks with one or two visible components can issue from the same implanted samples but with different observation conditions (incidence angle).
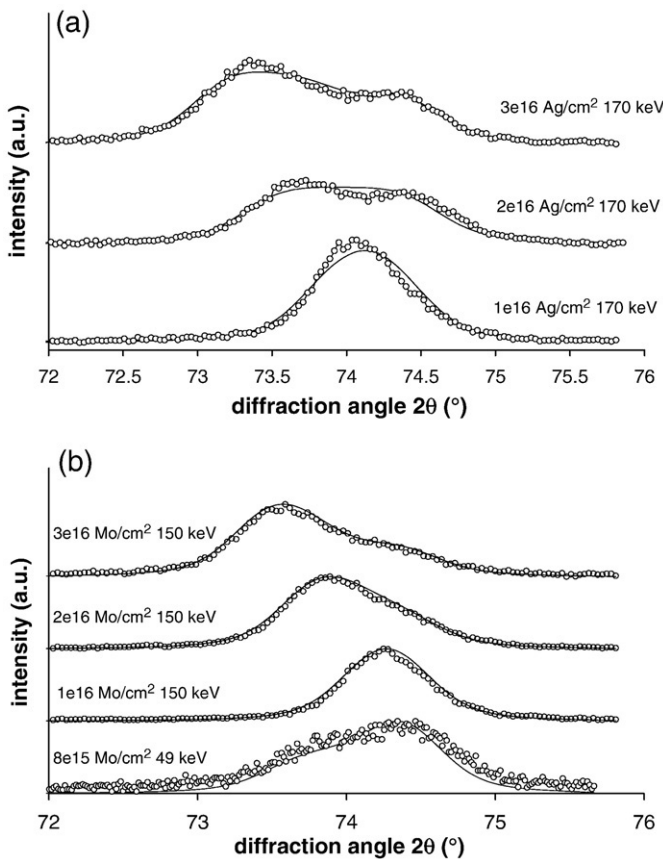
Acknowledgment

Fig. 9. Theoretical and experimental γ(220) peaks at 0.5° for 316LVM implanted with $1\cdot10^{16}$, $1.5\cdot10^{16}$, $2\cdot10^{16}$ Ag cm^{-2} at 170 keV(a), $8\cdot10^{15}$ Mo cm^{-2} at 49 keV, $1\cdot10^{16}$, $2\cdot10^{16}$, $3\cdot10^{16}$ Mo cm^{-2} at 150 keV (b).

References

[1] N. Mottu, M. Vayer, J. Dudognon, R. Erre, Surf. Coat. Technol. 200 (2005) 2131.
[2] E.I. Meletis, V. Singh, J.C. Jiang, J. Mater. Sci. Lett. 21 (2002) 1171.
[3] M.P. Fewell, D.R.G. Mitchell, J.M. Priest, K.T. Short, G.A. Collins, Surf. Coat. Technol. 131 (2000) 300.
[4] G.A. Collins, R. Hutchings, K.T. Short, J. Tendys, X. Li, M. Samadi, Surf. Coat. Technol. 74–75 (1995) 417.
[5] M. Guemmaz, A. Mosser, J.J. Grob, R. Stuck, Surf. Coat. Technol. 100–101 (1998) 353.
[6] C. Blawert, H. Halvelage, B.L. Mordike, G.A. Collins, K.T. Short, Y. Jiraskova, O. Schneeweiss, Surf. Coat. Technol. 136 (2001) 181.
[7] N. Mottu, M. Vayer, P. Andreazza, T. Sauvage, G. Blondiaux, R. Erre, Surf. Coat. Technol. 151–152 (2002) 47.
[8] M.E. Murphy, G.M. Insley, M.T. Laugier, S.B. Newcomb, Nucl. Instrum. Methods Phys. Res. B 234 (2005) 256.
[9] K. Marchev, R. Hidalgo, M. Landis, R. Vallerio, C.V. Cooper, B.C. Giesen, Surf. Coat. Technol. 112 (1999) 67.
[10] Y. Sun, X.Y. Li, T. Bell, J. Mater. Sci. 34 (1999) 4793.
[11] J.C. Jiang, E.I. Meletis, J. Appl. Phys. 88 (2000) 4026.
[12] J.P. Rivière, P. Meheust, J.P. Villain, C. Templier, M. Cahoreau, G. Abrasonis, L. Pranevicius, Surf. Coat. Technol. 158–159 (2002) 99.
[13] X. Xu, Z. Yu, L. Wang, J. Qiang, Z. Hei, Surf. Coat. Technol. 162 (2003) 242.
[14] J. Dudognon, M. Vayer, A. Pineau, R. Erre, Surf. Coat. Technol. 200 (2006) 5058.
[15] http://srim.org/.
[16] H.W. King, J. Mater. Sci. 1 (1966) 79.
[17] V.A. Lubarda, Mech. Mater. 35 (2003) 53.
[18] M.J. Marques, J. Pina, A.M. Dias, J.L. Lebrun, J. Feugeas, Surf. Coat. Technol. 195 (2005) 8.
[19] G. Abrasonis, J.P. Rivière, C. Templier, A. Declemy, S. Muzard, L. Pranevicius, Surf. Coat. Technol. 196 (2005) 262.
[20] N. Hayashi, T. Takahashi, Appl. Phys. Lett. 41 (1982) 1100.
[21] I. Sakamoto, N. Hyashi, B. Furubayashi, H. Tanoue, J. Appl. Phys. 68 (1990) 4508.
[22] S. Grigull, S. Parascandola, J. Appl. Phys. 88 (2000) 6925.
[23] S. Mändl, D. Manova, H. Neumann, M.T. Pham, E. Richter, B. Rauschenbach, Surf. Coat. Technol. 200 (2005) 104.
[24] F. Pedraza, J.L. Grosseau-Poussard, G. Abrasonis, J.P. Rivière, J.F. Dinhut, J. Appl. Phys. 94 (2003) 7509.
[25] D.L. Williamson, J.A. Davis, P.J. Wilbur, Surf. Coat. Technol. 103–104 (1998) 178.
[26] S. Rao, C.R. Houska, G. Grabowski, G. Ice, C.J. Sparks, J. Appl. Phys. 69 (1991) 8104.
[27] S. Rao, B.H. He, C.R. Houska, G. Grabowski, J. Appl. Phys. 69 (1991) 8111.